Journal of Advanced Research 29 (2021) 107–119

Contents lists available at ScienceDirect

Journal of Advanced Research

journal homepage: www.elsevier.com/locate/jare

Synthesis, microstructural characterization and nanoindentation of Zr, Zr-nitride and Zr-carbonitride coatings deposited using magnetron sputtering

Anwar Ul-Hamid

Center for Engineering Research, Research Institute, King Fahd University of Petroleum & Minerals, Dhahran 31261, Saudi Arabia

GRAPHICAL ABSTRACT

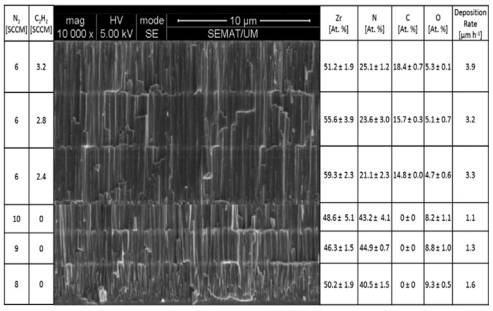

N_2 [SCCM]	C_2H_2 [SCCM]	Zr [At. %]	N [At. %]	C [At. %]	O [At. %]	Deposition Rate [µm h⁻¹]
6	3.2	51.2 ± 1.9	25.1 ± 1.2	18.4 ± 0.7	5.3 ± 0.1	3.9
6	2.8	55.6 ± 3.9	23.6 ± 3.0	15.7 ± 0.3	5.1 ± 0.7	3.2
6	2.4	59.3 ± 2.3	21.1 ± 2.3	14.8 ± 0.0	4.7 ± 0.6	3.3
10	0	48.6 ± 5.1	43.2 ± 4.1	0 ± 0	8.2 ± 1.1	1.1
9	0	46.3 ± 1.5	44.9 ± 0.7	0 ± 0	8.8 ± 1.0	1.3
8	0	50.2 ± 1.9	40.5 ± 1.5	0 ± 0	9.3 ± 0.5	1.6

ARTICLE INFO

Article history:
Received 8 June 2020
Revised 10 November 2020
Accepted 21 November 2020
Available online 25 November 2020

Keywords:
Nanoindentation
ZrN
ZC_2N
Magnetron sputter deposition
Hard coatings
Microstructure

ABSTRACT

Introduction: Hard coatings are primarily based on carbides, nitrides and carbonitrides of transition metal elements such as W, Ti, Zr, etc. Zr-based hard coatings show good resistance to wear, erosion, and corrosion as well as exhibit high hardness, high temperature stability, and biocompatibility, making them suitable candidates for tribological, biomedical, and electrical applications.
Objectives: The present study aims to synthesize uniform and adherent hard Zr-based coatings that demonstrate sound mechanical integrity.
Methods: Stainless steel (SS316) samples were coated with single layers of Zr, Zr-nitride, and Zr-carbonitride using magnetron sputter deposition technique. Deposition conditions were controlled to produce each coating with two different thickness i.e., 2 and 3 µm. Calotest was employed to confirm coatings thickness. Scanning electron microscope fitted with energy dispersive x-ray spectrometer was used to ascertain the morphology and elemental constitution of coatings. Cross-sectional samples were examined to ascertain coatings thickness and adhesion. X-ray diffractometer was employed for structural analysis. Instrumented nanoindentation hardness and elastic modulus were determined with nanoindenter. Ratio of nanohardness to elastic modulus was evaluated to observe the effect of coatings thickness on tribological behavior.
Results: Three coating compositions were produced namely hcp-Zr, fcc-ZrN and fcc-Zr_2CN. The highest hardness and elastic modulus were shown by ZrN coatings while pure Zr coatings showed the lowest values.
Conclusion: All coating compositions were found to be relatively uniform, continuous and adherent with no evidence of decohesion at the coating-substrate interface. Coatings produced in this study are thought to be suitable for tribological applications.

Peer review under responsibility of Cairo University.
E-mail address: anwar@kfupm.edu.sa

https://doi.org/10.1016/j.jare.2020.11.010
2090-1232/

Introduction

Wear resistant hard coatings are used to increase the service lifetime of cutting and drilling tools, biomedical implants, gas turbine engines, and household items, which encompass several industrial sectors such as manufacturing, oil and gas, power, medical, and defense. Hard coatings are usually based on carbides, nitrides and carbonitrides of transition metal elements such as Ti, Zr, W, etc. Zr-based coatings are comparatively difficult to deposit due to its relatively high melting point and low vapor pressure. These are also susceptible to contamination by oxygen and carbon during deposition process. For his reason, perhaps, comparatively smaller number of studies are found in the literature regarding Zr-based coatings. Due to its structure and bonding, Zr-based thin films exhibit high hardness, good biocompatibility, high temperature stability, and good resistance to wear, erosion, corrosion and oxidation, rendering them suitable candidates for use in tribological, nuclear fuel, corrosion-resistant, biomedical, electrical and decorative applications.

Over the years, various properties of Zr-nitride coatings have been investigated for a range of applications. It has been evaluated for its microhardness, adhesion and wear resistance in tribological applications and as a barrier material in integrated circuits [1–22], erosion protection for turbine and compressor blades [23–25], biocompatibility [26], optical and electrical properties [27–28], nuclear fuel element compatibility [29–31], and orientation dependence, microstructure, composition and corrosion [32–40]. Influence of synthesis parameters on coating properties have also been investigated [41–46]. Studies reported in the literature for Zr-carbonitride coatings are less in number. Properties and applications explored for Zr-carbonitrides include corrosion and oxidation resistance [47,48], composition, crystallinity and morphology [49], synthesis parameters [50], characterization [51], and optical [52] and biomedical [53–60] applications.

Hardness of Zr-carbide, Zr-nitride and Zr-carbonitride coatings reported in the literature varies between 12 and 19.6 GPa, 20–29 GPa and 10–31.3 GPa, respectively. Hardness depends on the synthesis technique, processing parameter, elemental concentration, and structure of coating produced. It is complicated to measure the hardness of coatings with small thickness due to the influence of underlying substrate. Nanoindentation makes it possible to measure small volumes of coatings by using small-sized indenters and very low loads such that the depth of penetration is kept in the order of tens or hundreds of nanometers only. Mechanical properties of coatings are determined without the need to visualize or measure the size of the indent. Analytical models are used to extract values of nanoindentation hardness and elastic modulus.

Magnetron sputter deposition technique produces adherent and uniform coatings and is popular in industry due to its cost effectiveness and reproducibility [61]. Relatively low temperature used during deposition allows for synthesis of coatings with improved properties.

In the present study, single layer coatings based on Zr, Zr-nitride and Zr-carbonitride constitution were developed using magnetron sputter deposition technique. Surface morphology and structure of the coatings were studied using scanning electron microscopy equipped with energy dispersive x-ray spectroscopy and x-ray diffraction. Surface mechanical properties such as nanoindentation hardness and modulus were measured using nanoindentation method. Load-displacement curves were obtained and the change in indentation hardness as a function of normal load was determined. Effect of carbon addition and film thickness was evaluated.

Materials and methods

Coatings synthesis

Single layers of Zr, Zr-nitride and Zr-carbonitride coatings (2 and 3 μm in thickness) were deposited on (100) Si wafers and stainless steel substrates (16 mm dia. disc, 3 mm in thickness) using magnetron sputter deposition technique. Coated Si wafers were later broken to study the fracture morphology of coatings in cross-section. Prior to deposition, the surface of stainless steel substrate was polished using emery paper (from 240 to 2400 grit) followed by mirror-polishing with a diamond suspension. The samples were then ultrasonically cleaned for 10 min in distilled water, followed by 10 min in ethanol and 10 min in acetone. Thereafter, in-situ sputter etching was performed, using a constant current of 480 mA for 900 s at 1.32 Pa Ar pressure. The coatings were produced by unbalanced dual magnetron sputtering. Coatings were deposited in reactive mode in $Ar/N_2/C_2H_2$ atmosphere, using two rectangular highly pure (99.2%) Zr targets (200×100 mm^2) placed on unbalanced type-2 magnetrons. The substrates were placed onto a rotational substrate holder using a matrix-like configuration.

The parameters for producing Zr, Zr-nitride and Zr-carbonitride were selected based on the composition, deposition rate and adhesion properties of each coating. The Zr current density was set between 1.8 and 2.0 A/cm^2, while the argon flux, bias voltage and chamber temperature were set to remain constant during depositions, i.e., at 60 sccm, −50 V and 100 °C, respectively. The base pressure, working pressure, target potential and other process parameters employed for deposition of final coatings are reported in table 1.

Three series of depositions were carried out to determine the most suitable synthesis parameters to achieve optimum coatings composition, thickness and adhesion. The parameters to deposit the second and third series of samples were selected based on the optimization carried out in the first series with some modification to compensate for excess Zr due to utilization of a new Zr target. As a result, the Zr current density was decreased and the gas fluxes were, in some cases, increased to attain similar composition and thickness compared with the first series of samples. Deposition rate was kept constant for each coating composition to enable an objective comparison between two coatings thickness used. Deposition rate decreased significantly for Zr-nitrides due to the introduction of nitrogen into the chamber which serves to poison the target and slow down deposition. The largest synthesis duration of 2.36 hrs was recorded for 3 μm ZrN coating.

Materials characterization

A scanning electron microscope (SEM model: JEOL JSM 6610LV) was used to examine the surface morphology of coatings. Secondary electron imaging was undertaken using SEM at an accelerating voltage of 20 kV. Surface morphology of coatings was examined in an as-received condition. The coated samples were cut with slow-cutting diamond wheel to minimize damage to the coating and mounted in cross-section using epoxy. This was followed by grinding with 600 grit size SiC paper and polishing with 1 μm diamond

Table 1
Designation, thickness and synthesis parameters used for each coating composition.

Sample ID	Coating Composition	Thickness [μm]	Deposition Rate [μm h^{-1}]	Ø C_2H_2 [sccm]	Ø N_2 [sccm]	Time [s]	Base Pressure [1 × 10^{-4}Pa]	Working Pressure [Pa]	Zr Target 1 Potential[V]	Zr Target 2 Potential [V]	Substrate Current [mA]
PN1	Zr	2.05	3.6 ± 0.1	0	0	2080	7.0	0.55	301	349	242
PN2	Zr	3.07	3.6 ± 0.1	0	0	3120	4.5	0.55	298	344	244
PN3	Zr-nitride	2.21 ± 0.04	1.40 ± 0.02	0	11	5700	4.3	0.54	335	376	246
PN4	Zr-nitride	3.3	1.40 ± 0.02	0	11	8500	5.3	0.54	333	373	241
PN5	Zr-carbonitride	2.17 ± 0.04	3.06 ± 0.01	3.2	6	2250	4.9	0.55	348.4	411.4	247.1
PN6	Zr-carbonitride	3.12	3.06 ± 0.01	3.2	6	3370	5.5	0.55	348.8	410.6	250.7

paste. The samples were sputtered with a thin layer of gold using a gold coater in argon environment. Thin coating of gold enhances surface conductivity of the sample and helps in reducing charge build-up during examination in the SEM. Elemental constitution of the coatings was determined with an energy dispersive x-ray spectrometer (EDS model: Oxford 50 mm^2 Si(Li) detector) fitted with an atmospheric thin window. Topography of Zr-based coatings was examined using contact mode atomic force microscopy (AFM model: Agilent 5500). An x-ray diffractometer (model: Rigaku Ultima IV XRD) with Cu Kα radiation (λ = 0.154 nm) was used in θ:θ configuration (diffraction angle 2θ range from 30° to 80°) to determine the phase constitution of coatings. Average crystallite size was determined with Scherrer equation $D = \frac{k\lambda}{\beta\cos\theta}$where k is a constant with a value of 0.89, λ = wavelength of x-rays (0.154 nm), β is broadening of peak at its full width half maximum (FWHM) in radians and θ is Bragg's diffraction angle.

Nanoindentation

A nanoindenter (Model: CSM Instruments) with a load range of 0.5 to 300 mN was used to undertake nanoindentation tests. A sharp three-faced pyramid Berkovich diamond tip was employed to enable penetration within small volumes. For each nanoindentation, tip was pushed into the sample at a fixed load and speed. Indentation was carried out at loads of 10 and 20 mN with load-unload speed of 20 mN/min. The time interval between load and unload cycle was 60 s. Continuous monitoring of applied normal load and displacement of indenter tip enabled plotting of load–displacement curve for each nanoindentation cycle. Hardness was calculated from the area of the indent which is derived from established geometry and size of the tip. Various analytical models have been put forward to calculate hardness and elastic modulus. These methods include Oliver and Pharr method [62,63], the deformation energy method [64–66], the force indentation function method [67–69], the Joslin-Oliver method [70,71] and the energy density method [72]. Most popular among these is Oliver and Pharr method which was employed in the present study.

Nanoindentation hardness (H) can be defined as the resistance to permanent deformation under an applied perpendicular load and is given by:

$H = \frac{P_{max}}{A_p}$ Pascalswhere

P_{max} = Maximum perpendicular load.
A_p = Projected contact area.

Elastic modulus (E) is given as:

$$E = \frac{1 - \upsilon_s{}^2}{\frac{1}{E_r} - \frac{1-\upsilon_i{}^2}{E_i}}$$

where

E_i = Elastic modulus of the tip.
E_r = Reduced modulus of the indentation contact.
υ_i = Poisson's ratio of the tip.
υ_s = Poisson's ratio of the test sample.

The values of hardness and elastic modulus data were obtained from real-time normal load versus displacement plots as recorded by the computer. Four indentations were taken at each load.

Experimental results

Coatings synthesis

Appropriate parameters for producing Zr, Zr-nitride and Zr-carbonitride coatings were selected using different N_2 and C_2H_2 flow rates in order to alter the nitrogen and carbon content in the films and determine the deposition rate and optimize coatings composition. An example demonstrating such optimization is shown for Zr-nitride and Zr-carbonitride coatings in Fig. 1a, where change in flow rates of N_2 and C_2H_2 resulted in different deposition rates, composition and coatings thickness. The deposition rate of coatings decreased when nitrogen was introduced into the process; such a behavior is expected due to the poisoning of Zr targets, while acetylene induced an increase in deposition rate compared with Zr-nitride coatings, which is explained by the ability of carbon to deposit directly onto coatings.

Less than 10 at.% oxygen was also detected as reported in Fig. 1a. The presence of oxygen may be attributed to high base pressure and atmospheric contamination of the deposition chamber [73]. Accumulation of oxygen within the chamber may become unavoidable at low deposition rates [74]. The films thickness obtained were in good agreement with the target thickness, with standard errors below 5%. A typical result is shown in Fig. 1b where Zr-carbonitride coating (2 μm in thickness) was obtained at a Zr-target current density of 1.8 A/cm^2 and N_2 and C_2H_2 flow rates of 6 sccm and 3.2 sccm, respectively.

It can be seen that the coatings exhibited primarily columnar growth with some fine grains at the coating-alloy interface (see Fig. 1a). This structure is typical of coatings formed with sputter deposition process which is carried out under conditions of high supersaturation giving rise to high nucleation rate and fine nuclei size at the base [75]. This is followed by grain boundary motion during coalescence and epitaxial growth giving rise to predominant columnar morphology observed in coatings studied here. This type of growth is supported by Thornton model where defects due to voided growth and atomic shadowing contribute to limited diffusion on sample surface [76]. Columnar morphology of Zr-based coatings has been reported in the literature [13].

Fig. 2 shows the relationship between target potential, chamber pressure and gas fluxes with respect to deposition time. Changes in targets potential and chamber pressure are clearly visible and are controlled by the amount of nitrogen present in the chamber.

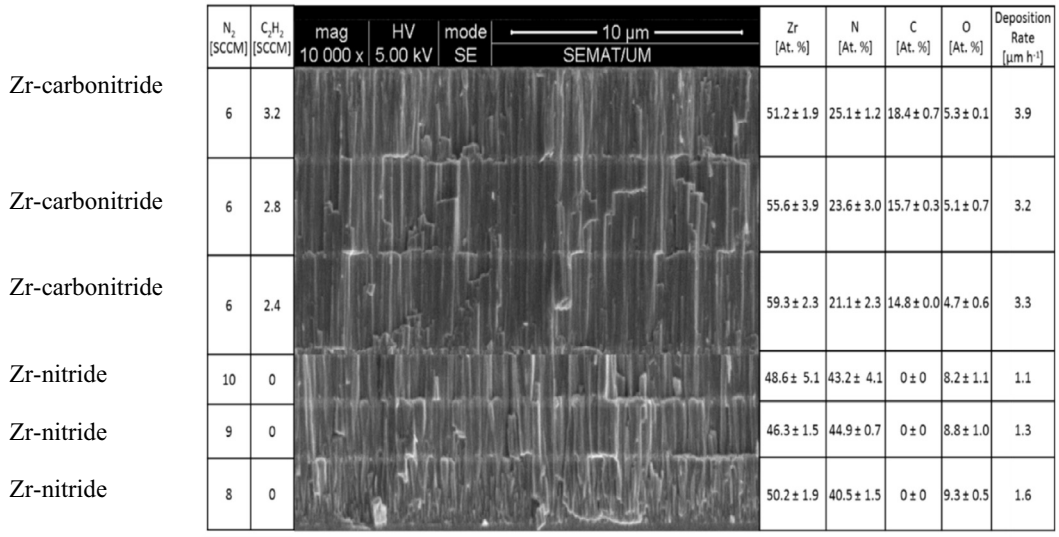

N_2 [SCCM]	C_2H_2 [SCCM]	Zr [At. %]	N [At. %]	C [At. %]	O [At. %]	Deposition Rate [µm h^{-1}]
6	3.2	51.2 ± 1.9	25.1 ± 1.2	18.4 ± 0.7	5.3 ± 0.1	3.9
6	2.8	55.6 ± 3.9	23.6 ± 3.0	15.7 ± 0.3	5.1 ± 0.7	3.2
6	2.4	59.3 ± 2.3	21.1 ± 2.3	14.8 ± 0.0	4.7 ± 0.6	3.3
10	0	48.6 ± 5.1	43.2 ± 4.1	0 ± 0	8.2 ± 1.1	1.1
9	0	46.3 ± 1.5	44.9 ± 0.7	0 ± 0	8.8 ± 1.0	1.3
8	0	50.2 ± 1.9	40.5 ± 1.5	0 ± 0	9.3 ± 0.5	1.6

(a)

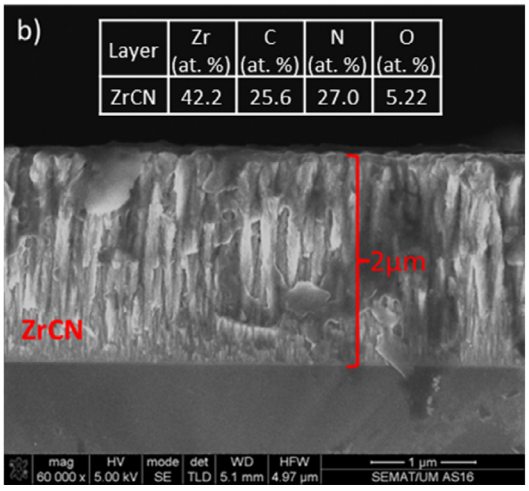

(b)

Fig. 1. (a) Change in flow rates of N_2 and C_2H_2 gas changes the deposition rate which alters the composition and thickness of Zr-nitride (bottom 3 rows) and Zr-carbonitride (top 3 rows) coatings. (b) High magnification SEM image showing 2 µm thick Zr-carbonitride layer obtained by controlling operational conditions within certain parameters. The compositions showed were obtained with SEM-EDS.

The targets potential typically increases as gas flux is increased; such an increment is explained by high reactivity of the surface of target with nitrogen and acetylene, thus poisoning the target surface for reactive magnetron sputtering. All coatings showed a variation in the target potential depending on the amount of gases introduced into the reactor.

The color of pure Zr coatings was silver grey, Zr-nitride was bright gold and Zr-carbonitride carried a dull gold color. This is in accordance with the literature where silver-colored metallic coatings have been reported for high Zr and low nitrogen contents [77,78]. Increase in nitrogen concentration in the coatings results in the formation of stoichiometric Zr-nitride that exhibits golden color [43,77,78].

The thickness of the coatings was evaluated using Calotest method where a rotating sphere of 20 mm in diameter was used at 900 rpm for 120 s to obtain the desired wear. The results are included in table 1, while the typical image obtained for each coating composition is presented in Fig. 3abc. This test also offered a qualitative method to evaluate the coatings adhesion to the substrates. The coatings that did not withstand the test were discarded and the synthesis conditions were adjusted to deposit coatings with improved adhesion. An example of the film failure after the Calotest is shown in Fig. 3d. A Zr interlayer between the substrate and functional layer was deposited for every composition in order to improve the adhesion, employing thickness between 250 and 300 nm. The coatings thickness are calculated for both Zr interlayer and the functional layer (Zr-nitride or Zr-carbonitride) where applicable.

Materials characterization

Scanning electron microscopy

Surface morphology was studied by examining the top surface of the coatings with a scanning electron microscope, as shown in Fig. 4 (a-f). It can be seen that all coatings exhibited a fairly uniform surface morphology. Coating grains were fine and spherical, which

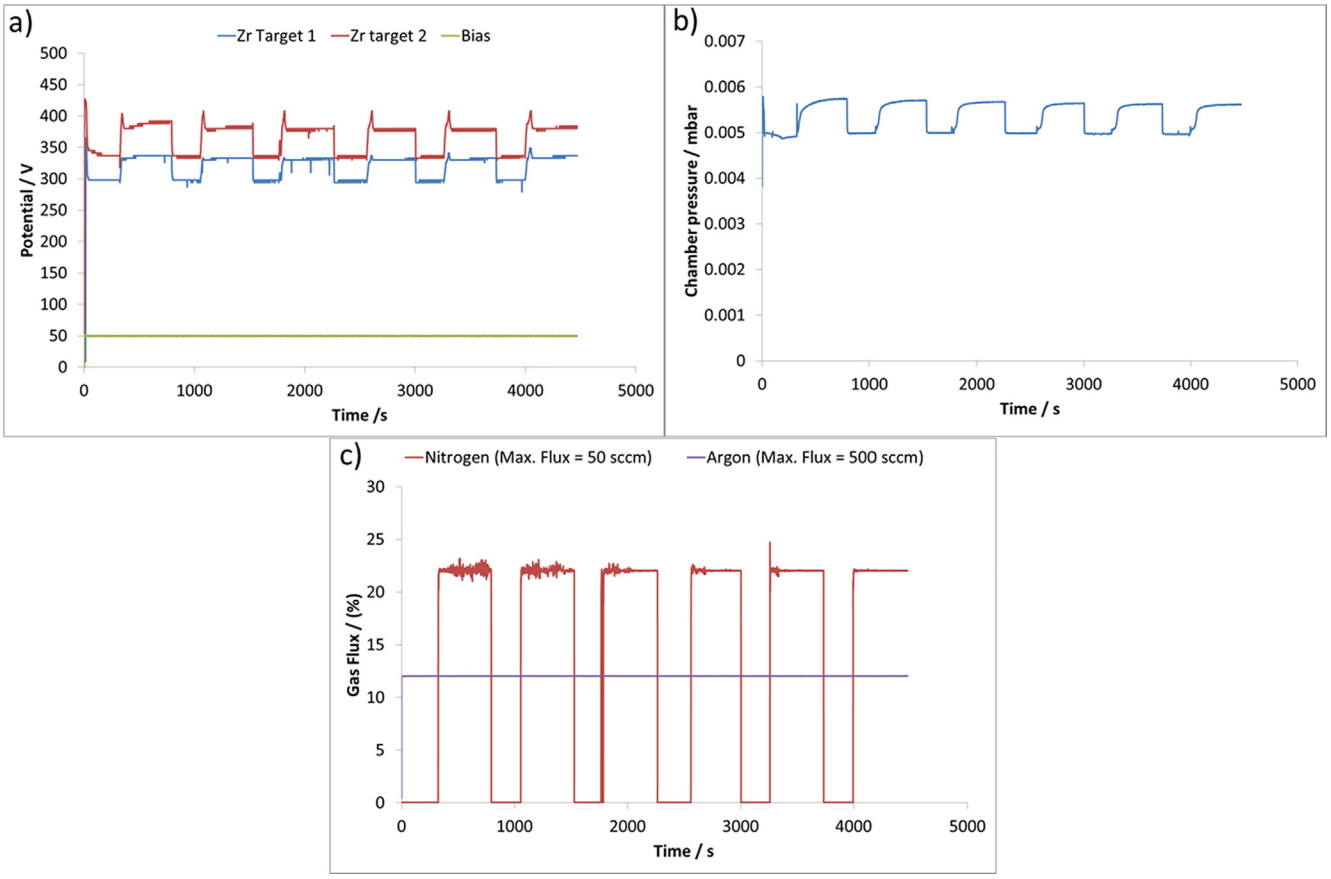

Fig. 2. Variables monitored during the sputtering process as a function of the deposition time. a) target and bias potential, b) chamber pressure and c) nitrogen and argon flux.

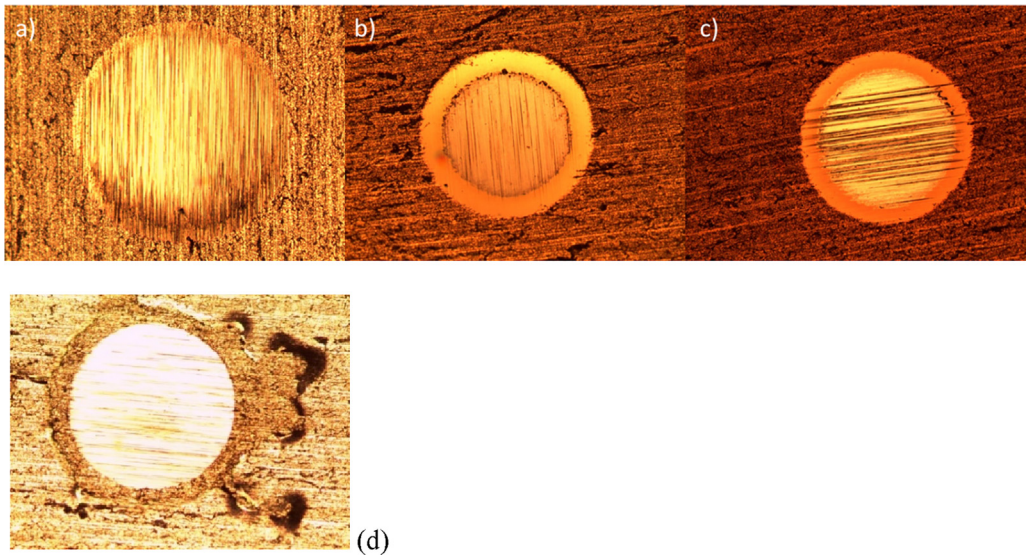

Fig. 3. Calotest images for a) Zr, b) Zr-nitride and c) Zr-carbonitride coatings. (d) Calotest image of a coating with poor adhesion.

corresponds with the columnar grain growth observed in Fig. 1. In addition to normal grain growth, localized grain agglomeration was also observed at the surface of thickening film promoted by the coalescence of adjacent grains. Coatings with 3 μm thickness showed relatively coarser grain size compared to those with 2 μm thickness for all coating compositions, as can be seen in table 2. This is due to grain growth that occurred in thicker (3 μm) coatings due to longer deposition times, which might allow adatoms to rearrange by surface diffusion and cause the grains to be larger.

It is also evident from Fig. 4a and b that grain size of coatings that are free of carbon and nitrogen is relatively large compared to coatings that contain these additions (as seen in Fig. 4c-f). Inclusion of carbon and nitrogen atoms within coatings serves to restrict grain growth by limiting the mobility of adjacent grains conferring

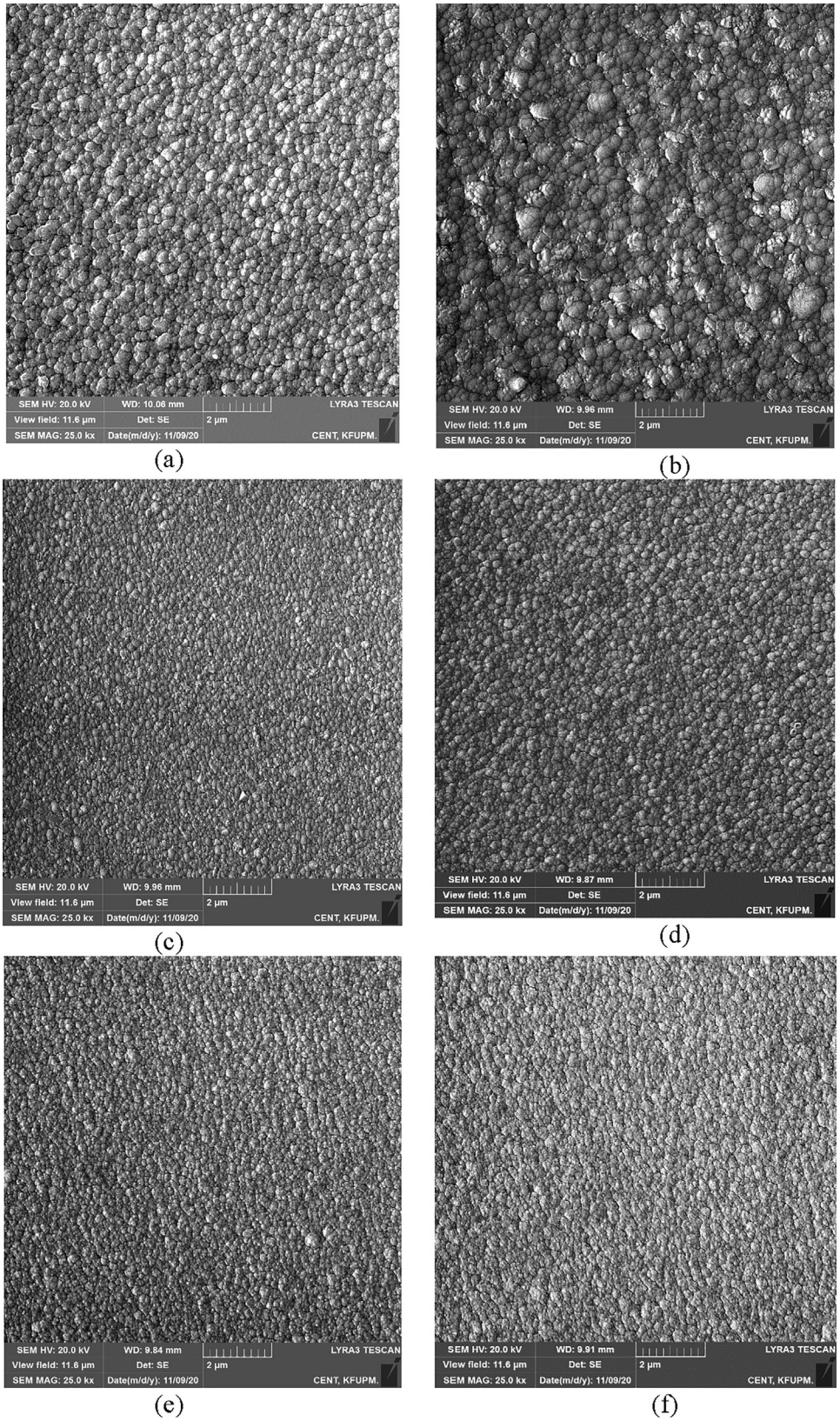

Fig. 4. High magnification SEM images of the top surface of coatings (a) Zr-2 µm, (b) Zr-3 µm, (c) Zr-nitride-2 µm, (d) Zr-nitride-3 µm, (e) Zr-carbonitride-2 µm, (f) Zr-carbonitride-3 µm.

them with fine grain size. Grain growth in Zr-carbonitride coatings with deposition time seems to be less significant due to the same reason (see Fig. 4e-f). Densification of coatings from Zr to Zr-nitride to Zr-carbonitride was observed also due to the presence of nitrogen and carbon in the film, as evident in high magnification SEM images shown in Fig. 4 (a-f). Interstitial positions are filled due

Table 2
Peak positions (2θ), identified phases and corresponding diffraction planes for each coating composition of Zr, Zr-nitride and Zr-carbonitride.

Sample ID	Peak position, 2θ (deg)	Identified phases and corresponding diffraction planes	Grain size, nm
		hcp Zr	
PN1 (Zr, 2 μm)	31.94	(100)	21.1 (PN1)
PN2 (Zr, 3 μm)	34.86	(002)	23.1 (PN2)
	36.48	(101)	
	47.98	(102)	
	56.85	(101)	
	63.51	(103)	
	68.66	−112	
	69.53	(201)	
		fcc ZrN	
PN3 (Zr-nitride, 2 μm)	33.63	−111	9.9 (PN3)
PN4 (Zr-nitride, 3 μm)	39.30	(200)	10.2 (PN4)
	56.37	(220)	
	67.70	−222	
		fcc Zr_2CN	
PN5 (Zr-carbonitride, 2 μm)	33.48	−111	7.6 (PN5)
PN6 (Zr-carbonitride, 3 μm)	38.86	(200)	7.6 (PN6)
	55.97	(220)	
	67.39	−222	
	70.60	−311	

to carbon and nitrogen diffusion reducing vacant spaces in the lattice. This results in higher densification and comparatively smoother morphology.

Fig. 5 shows cross-sectional SEM images of all coatings. It can be seen that the target thickness were well achieved by deposition conditions used. The Zr coating showed relatively high degree porosity while Zr-nitride and Zr-carbonitride coatings appear dense and pore-free. Typical EDS spectrum and x-ray mapping image obtained from a coated sample using SEM are shown in Fig. 6a and 6b, respectively.

X-ray diffraction

Zirconium nitride is a hard refractory ceramic material. It has fcc cubic structure and exhibits covalent bonding. Zirconium carbonitride is a quasi-binary solid solution that is formed when C and N atoms occupy the octahedral interstitial sites [79]. X-ray diffraction spectra obtained from all coating compositions are shown in Fig. 7. The phase constitution of coatings on samples PN1 and PN2 were identified as hcp Zr, PN3 and PN4 as cubic ZrN and PN5 and PN6 as cubic Zr_2CN, respectively. The details of peak positions for each coating is given in table 2. The formation of ZrN and Zr_2CN phases is corroborated by the elemental constitution detected using SEM-EDS analysis as shown in Fig. 1ab. Pure Zr coatings showed (200) preferred orientation while ZrN and Zr_2CN exhibited growth preference for (111) planes. Zr_2CN also exhibited a strong peak for (200) plane. Peaks in Zr_2CN shifted slightly toward lower 2θ values indicating increase in lattice parameter due to incorporation of carbon at interstitial sites in the lattice (see table 2). Preferred orientation of (200) in hcp Zr [77] and (111) in ZrN coatings has been reported in the literature [10,15,34]. As N_2 is introduced into the system, growth rate of (200) is inhibited due to lattice distortion or interstitial site occupancy by nitrogen atoms [77], resulting in (111) preferred orientation in Zr-nitride coatings. Preferred orientation exhibited by coatings depends on various factors including energy of ions used in deposition, gas flow rate, deposition rate, substrate bias voltage, substrate temperature, chamber pressure, deposition temperature, synthesis technique, coatings composition and thickness, etc. [80].

Grain size of the coatings reduced from 23.1 to 7.6 nm as N and C were introduced into the system. These values coincide with surface morphology of the coatings observed through SEM in Fig. 4a-f. As suggested earlier, carbon and nitrogen atoms restrict grain growth within coatings resulting in fine grain size.

Atomic force microscopy

Spherical grain morphology observed for all coating compositions using SEM was confirmed by two-dimensional images acquired with AFM as shown in Fig. 8a-f. The grain size became coarser and an increase in average surface roughness (Ra) was observed as the coating thickness was increased from 2 to 3 μm. The coatings also showed densification and smoother texture upon inclusion of C and N. Addition of C reduces roughness in Zr-based coatings as reported in the literature [81]. Also, (111) textured ZrN exhibits smooth surface morphology [82].

Nanoindentation

Nanoindentation of all coatings was carried out at two loads, e.g., 10 and 20 mN. For a typical plot, the change in applied normal force (e.g., load) and the penetration depth (e.g., displacement) of the indenter with time was obtained. The normal force was also plotted against penetration depth for the same indent. Penetration depth increased with load for all coating compositions and varied between 145 nm (for ZrN) and 435 nm (for pure Zr). The penetration depth of the indenter for ZrN and Zr_2CN coatings was within the recommended value of 10% of coating thickness. The penetration depth for pure Zr coatings varied from 11 to 20 % of coating thickness. This is due to the relatively low hardness exhibited by pure Zr coatings. Surface mechanical properties such as nanoindentation hardness and elastic modulus were calculated from these plots using Oliver & Pharr (O & P) method [62,63]. Values of nanohardness and elastic modulus obtained from each coating composition at 10 and 20 mN loads are plotted in the form of a bar chart in Fig. 9abc, respectively.

It can be seen in Fig. 9a that the lowest hardness was exhibited by pure Zr coatings (5–6 GPa) while ZrN showed the highest values of hardness (23–30 GPa). Zr_2CN coatings had intermediate hardness of 24–26 GPa. Keeping displacement of the indent to 10% of the coating thickness serves to reduce the influence of the substrate in hardness measurements. On the other hand, too small an indent might prove to be comparable in size to sample surface roughness compromising the accuracy of measurement. This will introduce an error in measurement data. To avoid this error, penetration depth is increased to at least 20x the surface roughness. Usually, a compromise is struck between these two competing conditions. At low loads, transition of the indented region from elastic to elastic/plastic state makes measurement more complicated [62]. Generally, for soft films on hard substrates, hardness values increase with increasing penetration depths of the indenter. For hard films on soft substrates, hardness will decrease with displacement.

In our study, hardness of all coatings decreases as the load is increased from 10 to 20 mN. At 10 mN, the contribution of SS316 substrate on coatings hardness is small. At 20 mN load, the influence of the substrate increases and results in lower hardness values for coatings. This indicates that the hardness of underlying SS316 substrate is lower than that of coatings used in this study. This is corroborated by the hardness values stated previously. Decrease in hardness with an increase in normal load indicates that the SS316 substrate yields at indentation depths smaller than the thickness of the coating. The hardness of uncoated bare SS316 alloy substrate was measured to be 2.10 GPa further corroborating

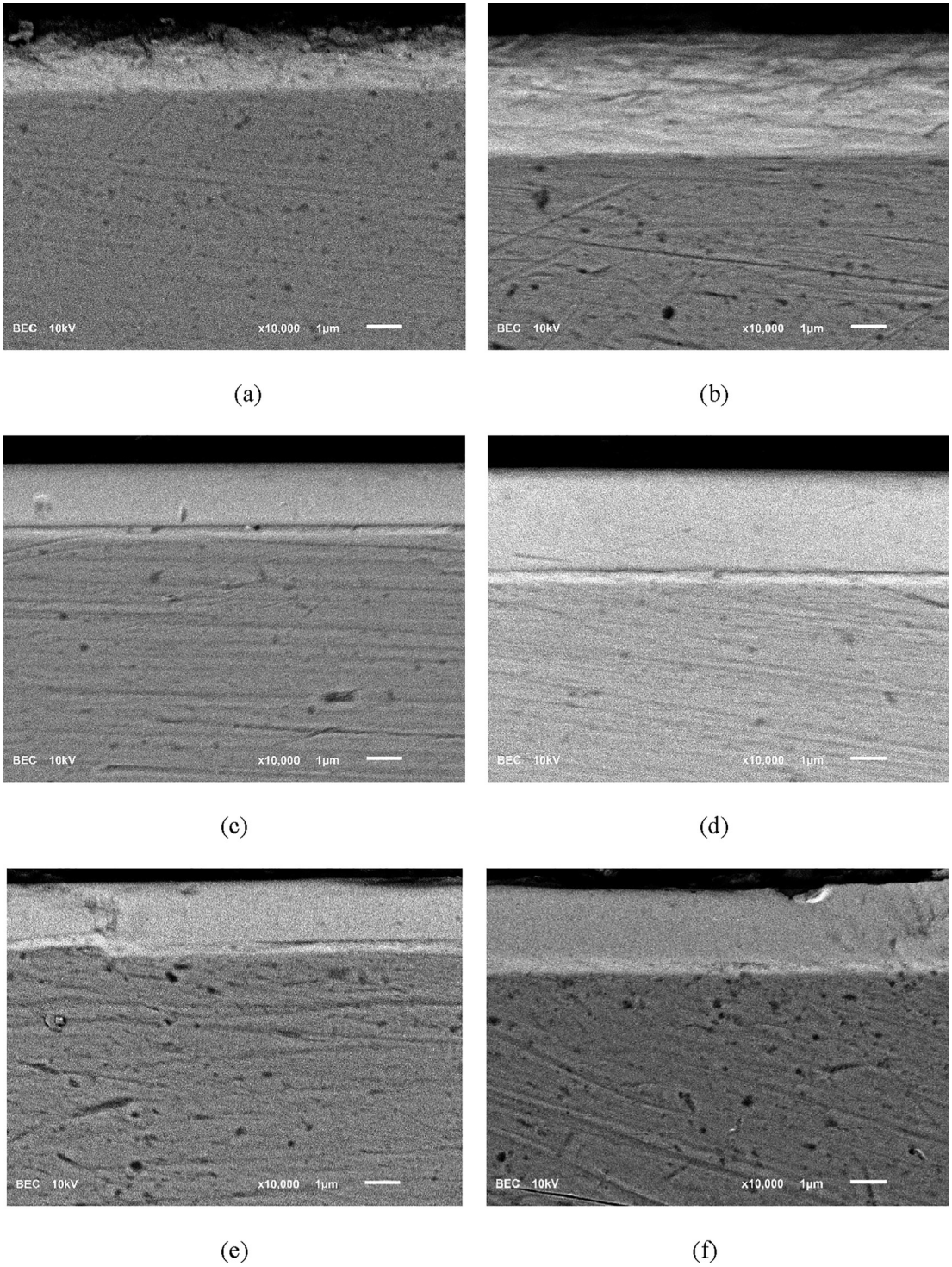

Fig. 5. Backscattered electron SEM images of cross-sectional samples for (a) Zr-2 μm, (b) Zr-3 μm, (c) Zr-nitride-2 μm, (d) Zr-nitride-3 μm, (e) Zr-carbonitride-2 μm, (f) Zr-carbonitride-3 μm.

the above observation. For a coating with larger thickness, the influence of substrate on coating hardness becomes smaller. This results in an increase in hardness for the 'hard' Zr coatings on 'soft' SS316 substrate at both 10 and 20 mN loads when coating thickness increases from 2 to 3 μm.

Elastic modulus follows the trend shown by hardness and decreases with normal load for all coatings (see Fig. 9b). It is higher for ZrN and Zr_2CN coatings with 2 μm thickness. Hardness to modulus (H/E) ratio is a good indicator of mechanical integrity of coatings [83–85]. Increase in coatings thickness serves to increase H/E ratio [86]. It can be seen in Fig. 9c that H/E values for ZrN and Zr_2CN coatings are comparable indicating similar degree of mechanical integrity. Pure Zr coatings exhibit lower H/E values.

Hardness of ZrC, Zr-nitride and Zr-carbonitride coatings reported in the literature varies widely. Hardness of Zr-carbides is 12–19.6 GPa, Zr-nitrides 20–29 GPa and Zr-carbonitrides 10–31.3 GPa. Hardness is affected by grain size, stoichiometry, defect density, structure, residual stress, and preferred orientation of

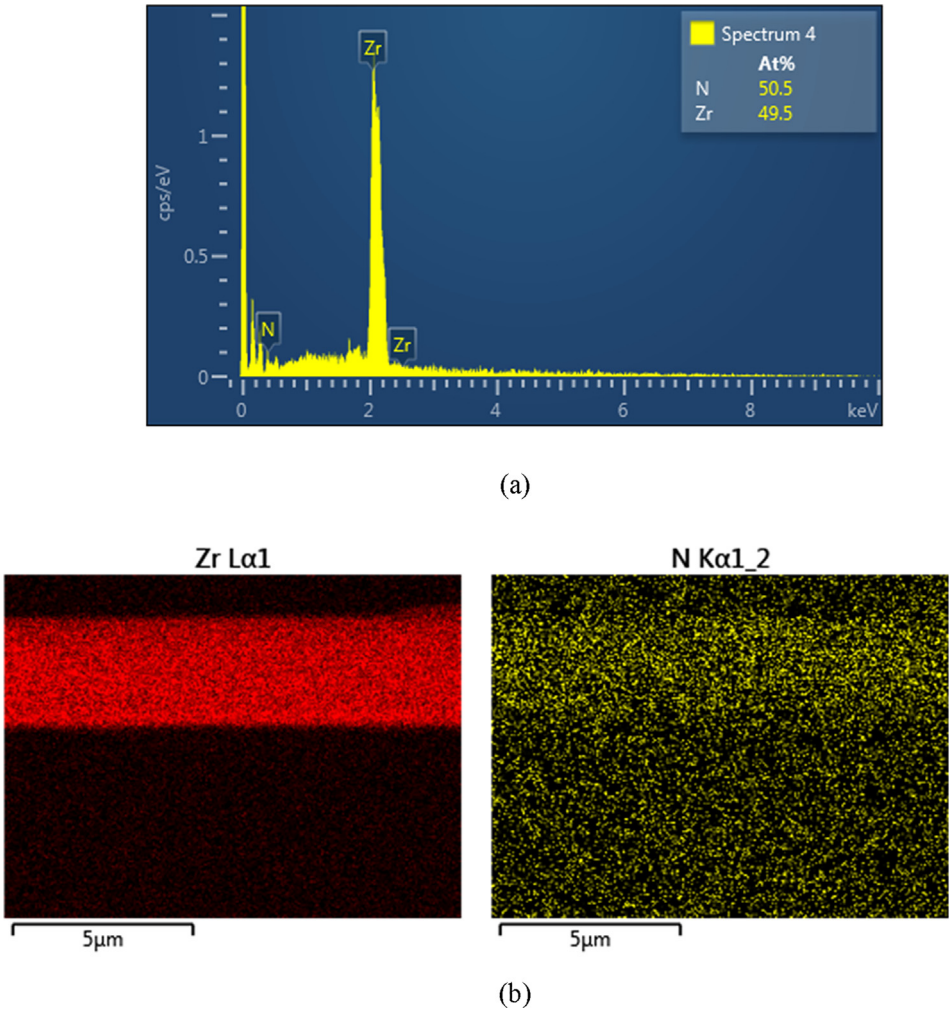

Fig. 6. (a) EDS spectrum and (b) X-ray maps of Zr and N obtained from the sample with ZrN coating (sample PN4). The atomic concentration of the sample coincides well with the target composition.

the coatings which in turn depends on synthesis technique and process parameters. Coatings with (111) texture are thought to exhibit high hardness due to its increased resistance to deformation and high activation energy for strain rate [87]. Dense nanostructured coatings are also believed to display high hardness [88]. In the present study, the highest hardness was exhibited by ZrN coatings which is thought to be due to its dense fine-grained structure and (111) texture. Zr_2CN coatings showed the lowest grain size (7.6 nm) but its hardness reduced slightly compared to ZrN coatings. This is attributed to inverse Hall-Petch effect where grain size less than 10 nm exhibits decreased hardness due to grain boundary sliding [89–93]. The effect of carbon on the hardness depends on its concentration [94]. Increase in hardness has been reported for small additions [95] while a reduction in hardness was observed for lower Zr/C ratios [81].

Conclusions

In this study, Zr-based nitride and carbonitride coatings were successfully produced via dc magnetron sputtering process using various flow rates of N_2 and C_2H_2 to control nitrogen and carbon concentrations in the coatings. Continuous and adherent Zr-based nitrides and carbonitrides with thicknesses set at 2 and 3 µm were deposited by controlling appropriate synthesis parameters. Elemental analysis confirmed the presence of carbon and nitrogen in addition to Zr. Increasing the flow rate of N_2 resulted in higher concentration of nitrogen in Zr-nitrides while similar behavior was observed for carbon in Zr-carbonitride coatings. Presence of carbon and nitrogen inhibited grain growth and resulted in more dense coatings. The morphological analysis revealed columnar grains accompanied by growth inhibition. Spherical morphology of surface grains and smooth texture of (111) planes upon addition of carbon and nitrogen were confirmed with AFM two-dimensional images. ZrN exhibited highest hardness (23–30 GPa) due to its fine grain size, dense structure and (111) preferred growth orientation. Zr_2CN showed slightly lower hardness due to inverse Hall-Petch effect. Pure Zr coating had the lowest hardness (5-6GPa). Elastic modulus of the coatings followed the hardness trend. In terms of elastic modulus and hardness, Zr-nitrides performed better than Zr-carbonitrides for both coatings thickness. Based on successful synthesis and attractive properties of Zr-nitrides and Zr-carbonitrides, these coatings are considered potential candidates for tribological applications.

Compliance with ethics requirements

This article does not contain any studies with human or animal subjects.

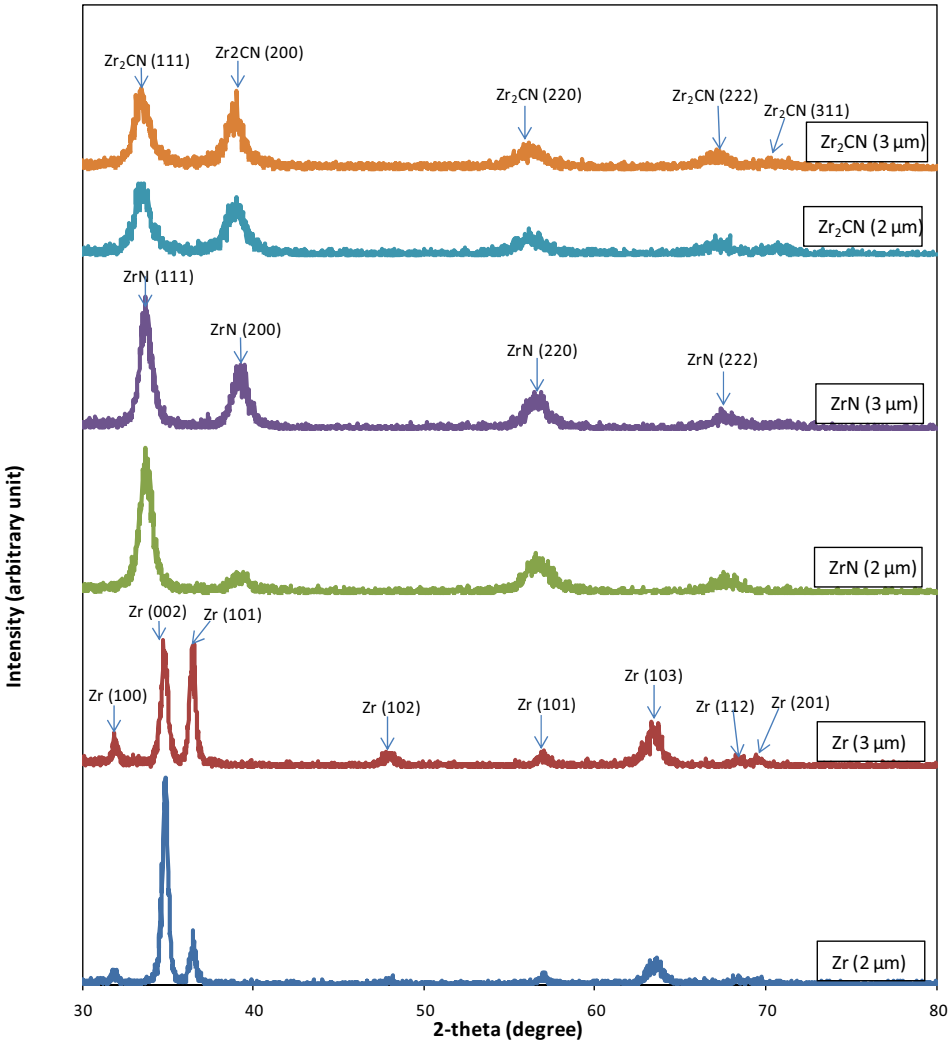

Fig. 7. Superimposed XRD spectra obtained from six samples with 3 different coating compositions identified as Zr, ZrN and Zr_2CN.

Declaration of Competing Interest

The authors declare that they have no known competing financial interests or personal relationships that could have appeared to influence the work reported in this paper.

Acknowledgement

Support provided by the Deanship of Scientific Research at the King Fahd University of Petroleum & Minerals, Dhahran, Saudi Arabia, through project number SB181002 is gratefully acknowledged.

References

[1] Duckworth RG. High purity sputtered tribological coatings. Thin Solid Films 1981;86(2–3):213–8.
[2] Sproul WD. Very high rate reactive sputtering of TiN. ZrN and HfN 1983;107:141.
[3] Duckworth RG. Sputtered coatings for metal finishing. Trans Inst Met Finish 1984;62(1):109–12.
[4] Duckworth RG. Backscattering analysis of ZrN alloys. Nucl Instrum Methods Phys Res 1986;B15:272–4.
[5] Simpson JCB, Earwaker LG. Nuclear analysis of zirconium nitride thin films. Nucl Instrum Methods Phys Res 1987;B24(25):701–4.
[6] Derradji A, Kassabji F. Preparation of plasma-sprayed coatings of ZrN under a controlled nitrogen atmosphere 1986;29:291–301.
[7] Valikhani M, Chandrashekhar S. Characteristics of TiN and ZrN Coatings on Split Point Drills Using the Static and Stochastic Models of the Force System as a Signature. Int J Adv Manuf Technol 1987;2(1):75–106.
[8] Musil J, Stepanek I, Musil JJ, Kolega M, Blahova O, Vyskocil J, et al. Properties of TiN, ZrN and ZrTiN coatings prepared by cathodic arc evaporation. Mater Sci Eng 1993;A163:211–4.
[9] Gruss K, Zheleva T, Davis R, Watkins T. Characterization of zirconium nitride coatings deposited by cathodic arc sputtering. Surf Coat Technol 1998;107:115–24.
[10] Ramana J, Kumar S, David C, Ray A, Raju V. Characterisation of zirconium nitride coatings prepared by DC magnetron sputtering. Mater Lett 2000;43:73–6.
[11] Sue J, Chang T. Friction and wear behavior of titanium nitride, zirconium nitride and chromium nitride coatings at elevated temperatures. Surf Coat Technol 1995;76–77:61–9.
[12] Lopez G, Staia M. High-temperature tribological characterization of zirconium nitride coatings. Surf Coat Technol 2005;200:2092–9.
[13] Meng Q, Wen M, Qu C, Hu C, Zheng W. Preferred orientation, phase transition and hardness for sputtered zirconium nitride films grown at different substrate biases. Surf Coat Technol 2011;205:2865–70.
[14] Singh A, Kumar N, Kuppusami P, Prasanthi T, Chandramohan P, Dash S, et al. Tribological properties of sputter deposited ZrN coatings on titanium modified austenitic stainless steel. Wear 2012;280–281:22–7.
[15] Valerini D, Signore M, Tapfer L, Piscopiello E, Galietti U, Rizzo A. Adhesion and wear of ZrN films sputtered on tungsten carbide substrates. Thin Solid Films 2013;538:42–7.
[16] Staia MH, Trocelis A, Zairi A, Suarez M, Puchi-Cabrera ES, Iost A, et al. Assessment of the mechanical and tribological performance of a ZrN PVD coating. Surf Eng 2019;35(6):491–500.
[17] Huang Sung-Hsiu, Tong Cheng-Yi, Hsieh Tsung-Eong, Lee Jyh-Wei. Microstructure and mechanical properties evaluation of cathodic arc deposited CrCN/ZrCN multilayer coatings. J Alloy Compd 2019;803:1005–15.

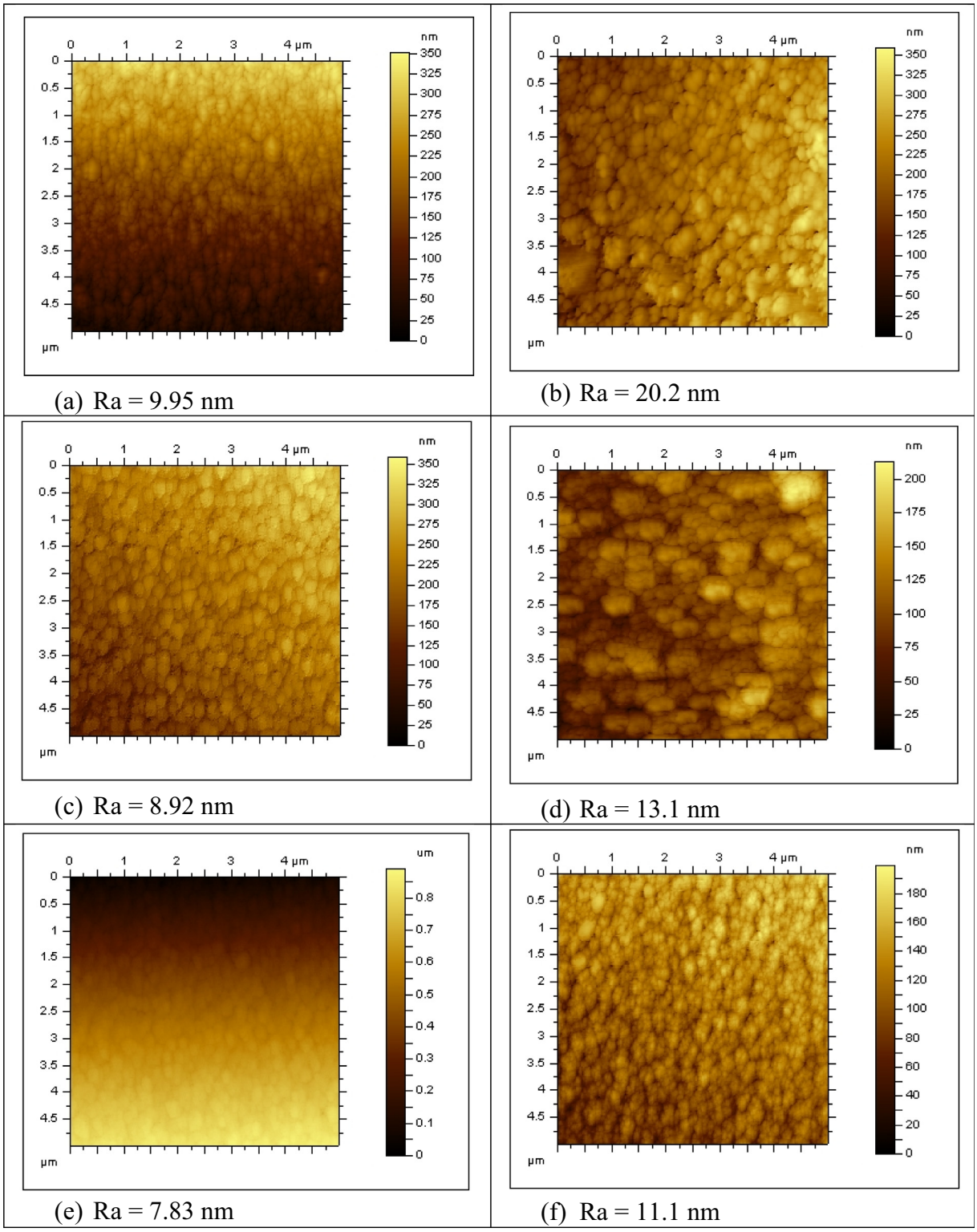

Fig. 8. AFM images obtained from the top surface (5x5 μm area) from (a) Zr-2 μm, (b) Zr-3 μm, (c) ZrN-2 μm, (d) ZrN-3 μm, (e) Zr_2CN-2 μm, (f) Zr_2CN-3 μm. Average surface roughness (Ra) for each coating composition was obtained at 13 different positions across the 5x5 μm region. The value quoted is the average Ra value obtained within the matrix scanned.

[18] El Azhari I, Garcia J, Soldera F, Suarez S, Jimenez-Pique E, Mucklich F, et al. Contact damage investigation of CVD carbonitride hard coatings deposited on cemented carbides. Int J Refract Metal Hard Mater 2020;86:105050.
[19] Guan Xiaoyan, Wang Yongxin, Xue Qunji. Effects of constituent layers and interfaces on the mechanical and tribological properties of metal (Cr, Zr)/ceramic (CrN, ZrN) multilayer systems. Appl Surf Sci 2020;502:144305.
[20] González-Carmona JM, Triviño JD, Gómez-Ovalle Á, Ortega C, Alvarado-Orozco JM, Sánchez-Sthepa H, et al. Wear mechanisms identification using Kelvin probe force microscopy in TiN, ZrN and TiN/ZrN hard ceramic multilayers coatings. Ceram Int 2020;46:24592–604.
[21] Krysina OV, Shugurov VV, Prokopenko NA, Petrikova EA, Tolkachev OS, Denisova YuA. Synthesis of single-layer ZrN-coatings using vacuum-arc

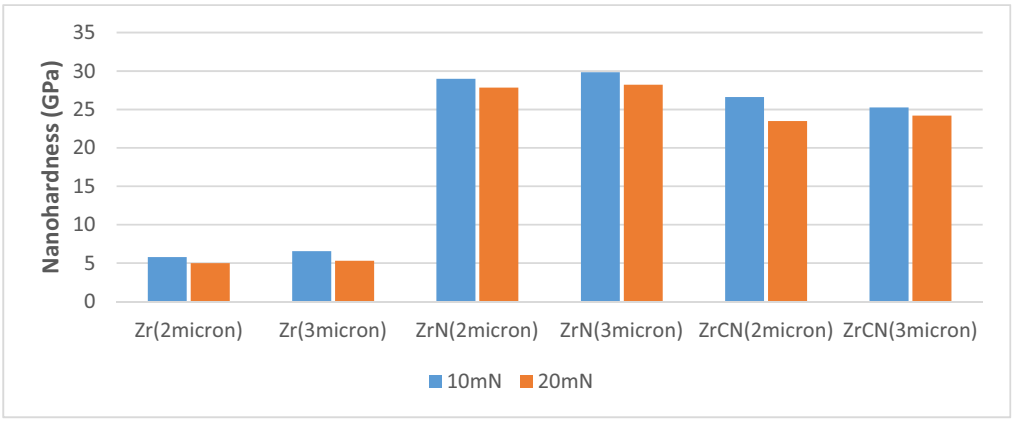

(a)

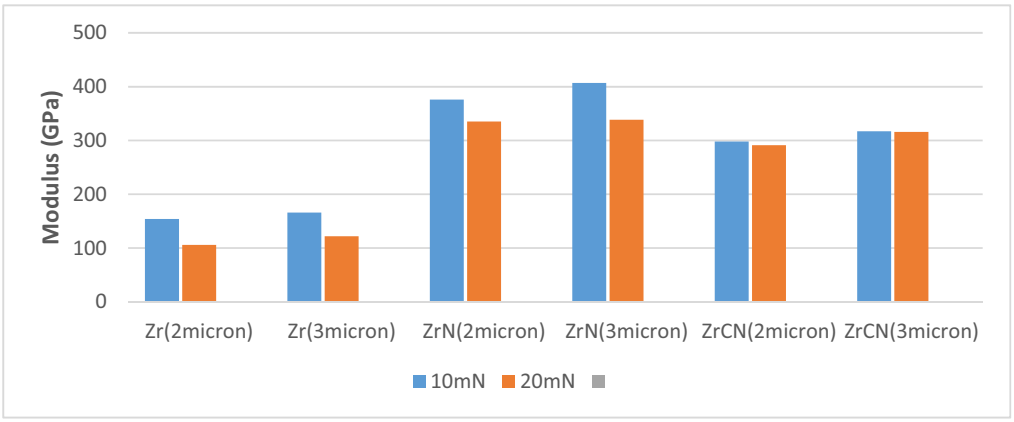

(b)

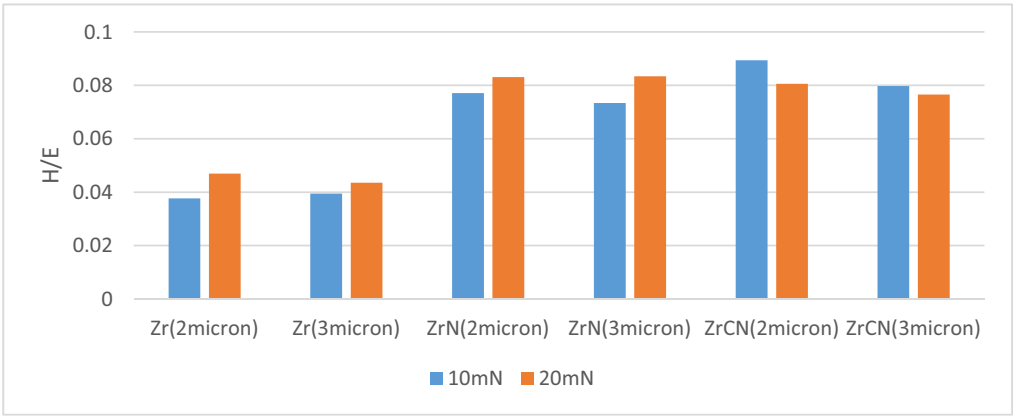

(c)

Fig. 9. Bar charts showing values of (a) nanohardness (b) elastic modulus (c) H/E values of all coating compositions.

plasma-assisted deposition with plasma flow filtering. Russ Phys J 2019;62(5):848–53.
[22] Kuznetsova T, Lapitskaya V, Warcholinski B, Gilewicz A, Chizhik S. Friction and wear of ZrN coatings under conditions of microcontact using atomic-force microscopy. J Frict Wear 2020;41(4):287–94.
[23] Sue JA, Trou HH. Zirconium nitride coated article and method for making same. Patent No CA 1992;1302807C.
[24] Muboyadzhyan SA. Erosion-Resistant Coatings for Gas Turbine Compressor Blades. Russian Metallurgy (Metally) 2009;2009(3):183–96.
[25] Zhang Yuechao, Jiang Xu, Cheng Lang, Zhao Yanjie, Peng Shuang, Jiang Shuyun. Exploring cavitation erosion resistance of ZrN nanocrystalline coating prepared by double-cathode glow discharge plasma technique. Vacuum 2020;182:109697.
[26] Davidson JA. Zirconium oxide and Zirconium nitride coated Biocompatible leads, Patent No. US005496359A (1996).
[27] Pilloud D, Dehlinger A, Pierson J, Roman A, Pichon L. Reactively sputtered zirconium nitride coatings: structural, mechanical, optical and electrical characteristics. Surf Coat Technol 2003;174–175:338–44.
[28] Patsalas Panos. Zirconium nitride: A viable candidate for photonics and plasmonics?. Thin Solid Films 2019;688:137438.
[29] Orlova EA, Gurbich AF, Molodtsov SL, Orlov VV, Bozin SN, Bashkin AV. Formation and investigation of nitride fuel compatible protective coatings on ferrite-martensite steel. At Energ 2008;105(5):344–50.
[30] Zhengtao Wu, Yiming Wu, Wang Qimin. A comparative investigation on structure evolution of ZrN and CrN coatings against ion irradiation. Heliyon 2019;5:e01370.

[31] Bhattacharya Sumit, Jamison Laura, Seidman David N, Walid Mohamed Y, Bei Michael J, Pellin Abdellatif M, et al. Nanocrystalline ZrN thin film development via atomic layer deposition for U-Mo powder. J Nucl Mater 2019;526:151770.
[32] Ma C-H, Huang J-H, Chena H. A study of preferred orientation of vanadium nitride and zirconium nitride coatings on silicon prepared by ion beam assisted deposition. Surf Coat Technol 2000;133–134:289–94.
[33] Matsuoka M, Isotani S, Sucasaire W, Kuratani N, Ogata K. X-ray photoelectron spectroscopy analysis of zirconium nitride-like films prepared on Si(100) substrates by ion beam assisted deposition. Surf Coat Technol 2008;202:3129–35.
[34] Roman D, Bernardi J, Amorim CLD, Souza FSD, Spinelli A, Giacomelli C, et al. Effect of deposition temperature on microstructure and corrosion resistance of ZrN thin films deposited by DC reactive magnetron sputtering. Mater Chem Phys. 2011;130: 147–53.
[35] Pei Chenrui, Deng Lijun, Liu Hongjin, He Zhen, Xiang Chengjie, Zhang Sam, et al. Corrosion inhibition behaviors of ZrNx thin films with varied N vacancy concentration. Vacuum 2019;162:28–38.
[36] Zhu Fei, Zhu Kangwei, Yin Hu, Ling Yunhan, Wang Dong, Peng Haiqing, et al. Microstructure and Young's modulus of ZrN thin film prepared by dual ion beam sputtering deposition. Surf Coat Technol 2019;374:997–1005.
[37] Maksakova Olga V, Webster Richard F, Tilley Richard D, Ivashchenko Volodymyr I, Postolnyi Bogdan O, Bondar Oleksandr V, et al. Nanoscale architecture of (CrN/ZrN)/(Cr/Zr) nanocomposite coatings: Microstructure, composition, mechanical properties and first principles calculations. J Alloy Compd 2020;831:154808.
[38] Huang Jia-Hong, Kuo Kun-Lin, Ge-Ping Yu. Oxidation behavior and corrosion resistance of vacuum annealed ZrN-coated stainless steel. Surf Coat Technol 2019;358:308–19.
[39] Mareus Rubenson, Mastail Cedric, Anğay Fırat, Brunetiere Noel, Abadias Gregory. Study of columnar growth, texture development and wettability of reactively sputter-deposited TiN, ZrN and HfN thin films at glancing angle incidence. Surf Coat Technol 2020;399:126130.
[40] Kuznetsova TA, Lapitskaya VA, Warcholinski B, Gilewicz A, Shabliuk AV, Chizhik SA. The influence of the zirconium sub layer thickness on the surface microstructure of the magnetron ZrN coatings. J Phys: Conf Ser 2019;1281:012046.
[41] Singh A, Kuppusami P, Khan S, Sudha C, Thirumurugesan R, Ramaseshana RDR, et al. Influence of nitrogen flow rate on microstructural and nanomechanical properties of Zr–N thin films prepared by pulsed DC magnetron sputtering. Appl Surf Sci 2013;280:117–23.
[42] Muneshwar T, Cadien K. Comparing XPS on bare and capped ZrN films grown by plasma enhanced ALD: Effect of ambient oxidation. Appl Surf Sci 2018;435:367–76.
[43] Calderon SV, Oliveira JC, Martinez-Martinez D, Cunha L, Rodrigues M, Borges J. Zr-O-N coatings for decorative purposes: Study of the system stability by exploration of the deposition parameter space. Surf Coat Technol 2018;343:30–7.
[44] Rauchenwald Elisabeth, Lessiak Mario, Weissenbacher Ronald, Haubner Roland. Chemical vapor deposition of ZrN using in situ produced ZrCl4 as a precursor. Ceram Int 2019;45:9410–4.
[45] Mahmood K, Bashir S, Faizan-ul-Haq M, Akram A, Hayat M Shahid, Rafique A Mahmood. Surface, structural, electrical and mechanical modifications of pulsed laser deposited ZrN thin films by implantation of MeV carbon ions. Nuclear Inst Methods Phys Res B 2019;448:61–9.
[46] Kuznetsova T, Lapitskaya V, Khabarava A, Chizhik S, Warcholinski B, Gilewicz A. The influence of nitrogen on the morphology of ZrN coatings deposited by magnetron sputtering. Appl Surf Sci 2020;522:146508.
[47] Sintsova IT, Kbzlovskii LV. Mechanical properties and corrosion resistance of steels with titanium and zirconium carbonitride coatings. Prot Met 1970;6 (5):567–70.
[48] Caillet M, Ayedi HF, Besson J. Etude de la corrosion de revetements refractaires sur le zirconium III. Oxydation pr la vapeur d''eau de revetements de nitrure et de carbonitrure de zirconium. J Less Common Metals 1978;58:37–46.
[49] Berndt H, Zeng A-Q, Stock H-R, May P. Zirconium carbonitride films produced by plasma-assisted metal organic chemical vapour deposition. Surf Coat Technol 1995;74–75:369–74.
[50] Grigore E, Ruset C, Li X, Dong H. Zirconium carbonitride films deposited by combined magnetron sputtering and ion implantation (CMSII). Surf Coat Technol 2010;204:1889–92.
[51] Calderon SV, Cavaleiro A, Carvalho S. Chemical and structural characterization of Zr C N Ag coatings:XPS, XRD and Raman spectroscopy. Appl Surf Sci 2015;346:240–7.
[52] Usmani B, Vijay V, Chhibber R, Dixit A. Effect of Growth Condition on Mechanical Properties of Zirconium Carbonitride Absorber-Based Spectrally Selective Coatings. In: Concentrated Solar Thermal Energy Technologies, L. Chandra and A. Dixit, Eds., (2018) p. 137–43.
[53] Calderon SV, Galindo RE, Oliveira J, Cavaleiro A, Carvalho S. Ag+ release and corrosion behavior of zirconium carbonitride coatings with silver nanoparticles for biomedical devices. Surf Coat Technol 2013;222:104–11.
[54] Calderon SV, Oliveira J, Evaristo M, Cavaleiro A, Carvalho S. Prediction of optimized composition for enhanced mechanical andelectrochemical response of Zr-C-N-Ag coatings for medical devices. Appl Surf Sci 2014;320:570–80.
[55] Ferreri I, Lopes V, Calderon SV, Tavares C, Cavaleiroc A, Carvalho S. Study of the effect of the silver content on the structural and mechanical behavior of Ag-ZrCN coatings for orthopedic prostheses. Mater Sci Eng C 2014;42:782–90.
[56] Wang L, Zhao X, Ding M, Zheng H, Zhang H, Zhang B, et al. Surface modification of biomedical AISI 316L stainless steel withzirconium carbonitride coatings. Appl Surf Sci 2015;340:113–9.
[57] Ferreri I, Calderon SV, Galindo RE, Palacio C, Henriques M, Piedade A, Carvalho S. Silver activation on thin films of Ag–ZrCN coatings for antimicrobial activity. Mater Sci Eng C 2015;55:547–55.
[58] Calderon SV, Cavaleiro A, Carvalhoa S. Electrochemical response of ZrCN-Ag-a (C, N) coatings in simulated body fluids. Electrochimica Acta 2015;176:898–906.
[59] Calderon SV, Ferreri I, Henriques M, DeHosson J, Cavaleiro A, Carvalho S. Nano-galvanic coupling for enhanced Ag+ release in ZrCN-Ag films: Antibacterial application. Surf Coat Technol 2016;298:1–6.
[60] Yao S-H, Su Y-L, Lai Y-C. Antibacterial and Tribological Performance of Carbonitride Coatings Doped with W, Ti, Zr, or Cr Deposited on AISI 316L Stainless Steel. Materials 2017;10:1189.
[61] Greene JE. Review Article: Tracing the recorded history of thin-film sputter deposition: From the 1800s to 2017, Journal of Vacuum Science & Technology A 35 (2017), 05C204; http://doi.org/10.1116/1.4998940. Retrieved 6 Sept. 2018.
[62] Oliver WC, Pharr GM. J Mater Res 1992;7:1564.
[63] Pharr GM. Mater Sci Eng A 1998;253:151.
[64] Rother B, Dietrich DA. Surf Coat Technol 1995;74–75:614.
[65] Li X, Diao D. Acta Mater 1997;45(11):4453.
[66] Veprek S. Invited Paper, International Conference on Trends and Applications of Thin Films, TAFT 2000. France: Nancy; March 2000.
[67] Karvankova P, Manning HD, Eggs C, Veprek S. Surf Coat Technol 2001;146–147:280.
[68] Friedrich C, Berg G. Thin Solid Films 1996;290–291:216.
[69] Musil J, Kunc F. Surf Coat Technol 2002;154:304.
[70] Saha R, Nix WD. Mater Sci Eng A 2001;319–321:898.
[71] Saha R, Nix WD. Acta Mater 2002;50:23.
[72] Rother B, Lunow T, Leonhardt G. Surf Coat Technol 1995;71:229.
[73] Silva E, Rebelo de Figueiredo M, Franz R, Escobar Galindo R, Palacio C, Espinosa A, et al. Structure-property relations in ZrCN coatings for tribological applications. Surf Coatings Technol 2010;205:2134–41.
[74] Oliveira A, Cavaleiro A, Vieira MT. Production and characterization of Si-N films obtained by r.f. magnetron sputtering. Surf Coatings Technol 1993;60(1–3):463–7.
[75] Thompson CV, Carel R. Texture development in polycrystalline thin films. J Mater Sci Eng 1955;32(3):211–9.
[76] Thornton JA. High rate thick film growth. Annu Rev Mater Sci 1977;7:239–60.
[77] Liu C-P, Yang H-G. Systematic study of the evolution of texture and electrical properties of ZrN x thin films by reactive DC magnetron sputtering. Thin Solid Films 2003;444:111.
[78] Ul-Hamid A. The effect of deposition conditions on the properties of Zr-carbide, Zr-nitride and Zr-carbonitride coatings – a review. Mater Adv 2020;1:988–1011.
[79] Harrison RW, Lee WE. Processing and properties of ZrC, ZrN and ZrCN ceramics: a review. Adv Appl Ceram 2016;115(5):294–307.
[80] Ul-Hamid A. Microstructure, properties and applications of Zr-carbide, Zr-nitride and Zr-carbonitride coatings: a review. Mater Adv 2020;1:1012–37.
[81] Meng Q, Wen M, Mao F, Nedfors N, Jansson U, Zheng W. Deposition and characterization of reactive magnetron sputtered zirconium carbide films. 232;2013:876–83.
[82] Farkas N, Zhang G, Ramsier R, Evans E, Dagata J. Characterization of zirconium nitride films sputter deposited with an extensive range of nitrogen flow rates. J Vac Sci Technol A 2008;26:297.
[83] Leyland A, Matthews A. Wear 2000;246:1.
[84] Gao JP, Luedtke WD, Landman U. Science 1995;270:605.
[85] Batista JCA, Godoy C, Pintaude G, Sinatora A, Matthews A. Surf Coat Technol 2003;174–175:891.
[86] Beake BD, Ranganathan N. Mater Sci Eng, A 2006;423:46–51.
[87] Swygenhoven HV, Spacz M, Care A. Role of low and high angle grain boundaries in the deformation mechanism of nanophase Ni: A molecular dynamics simulation study. NanoStruct Mater 1998;10(5):819–28.
[88] Craciun V, McCumiskey E, Hanna M, Taylor C. Very hard ZrC thin films grown by pulsed laser deposition. J Eur Ceram Soc 2013;33:2223–6.
[89] Scattergood R, Koch C. Scr Metall Mater 1992;27:1195.
[90] Gryaznov V, Gutkin M, Romanov A, Trusov L. J Mater Sci 1993;38:4359.
[91] Wang N, Wang Z, Aust K, Erb U. Acta Metall Mater 1995;43:519.
[92] Takeuchi S. Scr Mater 2001;44:1483.
[93] Shimokawa T, Nakatani A, Kitagawa H. Phys Rev B 2005;71(71):224110.
[94] He X-M, Shu L, L H-B, Li H-D. Structural characteristics and hardness of zirconium carbide films prepared by tri-ion beam-assisted deposition, J Vac Sci Technol A, 16(4) (1998), 2337.
[95] Bruckner J, Mantyla T. Reactive magnetron sputtering of zirconium carbide films using Ar-CH4 gas mixtures. Surf Coat Technol 1993;59:166–70.